Environmental Science Nano

# Nanoconfinement Matters in Humidified CO2 Interaction with Metal Silicates



| | |
|---|---|
| Journal: | *Environmental Science: Nano* |
| Manuscript ID | EN-ART-02-2022-000148.R1 |
| Article Type: | Paper |
| | |

**Environmental Significance:**

Nanoconfined environments in the structure of natural and synthetic metal-siliciates alters the bulk phase behavior of wet $CO_2$-rich fluid mixtures and could impact the carbonation reaction rate in nano-porous geological materials and construction waste. This study shows that regardless of $CO_2$ pressure, pore size, and surface chemistry, a nanometer thick water layer persists on the surface of metal-silicates even below the saturation level. Moreover, it is shown that $CO_2$ molecules could reach the surface of calcium-silicate-hydrate and react with surface water and hydroxyl group to produce carbonic acid and bicarbonate with a relatively low energy barrier. The presence of adsorbed water film and surface carbon speciation in nanoconfined environments signify the benefits of carbon sequestration with humidified $CO_2$- rich fluids.

# Nanoconfinement Matters in Humidified $CO_2$ Interaction with Metal Silicates

Siavash Zare[1], K.M. Salah Uddin[2], Andreas Funk[2,3], Quin R.S. Miller, Mohammad Javad Abdolhosseini Qomi[1,*]

[1]Department of Civil and Environmental Engineering, Henry Samueli School of Engineering, E4130 Engineering Gateway, University of California, Irvine, Irvine, CA, 92697-2175, USA.
[2] Department of Civil Engineering, University of Kassel, Germany, Mönchebergstraße 19, 34125 Kassel, Germany.
[3]Chemistry Department, University of Siegen, Adolf-Reichwein-Straße 2, 57068 Siegen, Germany.
[4]Physical and Computational Sciences Directorate, Pacific Northwest National Laboratory, Richland, WA, USA.

**Abstract:** With enigmatic observations of enhanced reactivity of wet $CO_2$-rich fluids with metal silicates, the mechanistic understanding of molecular processes governing carbonation proves critical in designing secure geological carbon sequestration and economical carbonated concrete technologies. Here, we use the first principle and classical molecular simulations to probe the impact of nanoconfinement on physicochemical processes at the rock-water-$CO_2$ interface. We choose nanoporous calcium-silicate-hydrate (C-S-H) and forsterite ($Mg_2SiO_4$) as model metal silicate surfaces that are of significance in the cement chemistry and geochemistry communities, respectively. We show that while a nanometer-thick interfacial water film persists at undersaturated conditions consistent with *in situ* infrared spectroscopy, the phase behavior of the water-$CO_2$ mixture changes from its bulk counterpart depending on the surface chemistry and nanoconfinement. We also observe enhanced solubility at the interface of water and $CO_2$ phases, which could amplify the $CO_2$ speciation rate. Through free energy calculations, we show that $CO_2$ could be found in a metastable state near the C-S-H surface, which can potentially react with surface water and hydroxyl groups to form carbonic acid and bicarbonate. These findings support the explicit consideration of nanoconfinement effects in reactive and non-reactive pore-scale processes.

**Keywords:** Carbon mineralization, nanoconfinement, molecular simulation, metal silicates, reactivity

## Introduction:

Carbonation of Mg- and Ca-rich silicates promises scalable solutions to mitigate the calamitous impacts of anthropogenic carbon emissions. These solutions can be realized in geological settings through *in situ* carbonation of mafic and ultramafic lithologies[1–3], or above ground through well-controlled *ex situ* carbon mineralization facilities to produce value-added concrete products[4]. The potential *in situ* $CO_2$ storage capacity of continental flood basalts[5], oceanic igneous plateaus[6,7], and basalt ridges[8,9] is greater by an order of magnitude than the estimated $CO_2$ emissions from burning all fossil fuel resources on Earth.[3] Ultramafic tailings[10,11], alkaline industrial residues[12], construction and demolition waste[13,14] and naturally occurring minerals such as olivine[15], can also collectively offset up to 30 Gt of emissions a year via *ex situ* proccesses.[16]

Whether realized *in* or *ex situ*, the permanent $CO_2$ conversion to carbonate minerals is advantageous over storage through residual trapping in nonreactive sedimentary formations.[17,18] However, the carbon mineralization extent and associated costs should be optimized to engender maximal $CO_2$ uptake through a rapid and close-to-complete carbonation process. Therefore, it is critical to predict the carbonation processes, including rates and mechanisms, as they directly affect

*Corresponding author: mjaq@uci.edu

storage security, efficiency, and cost. Despite this urgency, our understanding of carbon mineralization kinetics and underlying molecular pathways, especially with humidified $CO_2$-rich fluids, remain limited.

A major challenge in determining the carbonation rate is the complexity arising from confinement effects on fluid-rock and fluid-fluid interactions in the pore space. Compared to the bulk phase, confined fluids express substantially different physicochemical attributes and reaction rates.[19–21] For instance, recent experiments highlight the distinct thermodynamic properties of fluid in shales[22–24], model nanoporous glasses[25], and mesoporous silicon[26]. When confined in nanoporosity, fluid-solid interaction can also significantly impact the fluid phase behavior, sorption, capillary condensation, wettability, and imbibition.[27–30] Based upon experiments performed on mesoporous silicon[26], a follow-up theoretical study[27] showed that imbibition occurs when the relative humidity is above a critical value, well below the vapor saturation pressure. The fluid mixture phase behavior in the porous rock is particularly significant as it remains unclear to what extent the classical bulk aqueous-mediated dissolution-precipitation pathways can be applied to water-poor systems. Understanding wettability is also critical given its influences on sealing rock effectiveness[31,32] and storage efficiency in a subsurface carbon storage scenario, including in mafic geologic formations[33,34].

In this work, we study nanoconfined water-$CO_2$ mixtures on two model metal silicates with wide-ranging environmental and technological significance: 1) forsterite ($Mg_2SiO_4$), the magnesium endmember of olivine, relevant to carbonation studies of mafic (e.g. basalt) and ultramafic (e.g. peridotite) lithologies, and 2) Calcium-Silicate-Hydrate (C-S-H), the binding phase in the cement paste that is responsible for concrete's strength, fracture, and durability properties.[35–37] Carbonation of concrete infrastructure is estimated to be the sink for about 2.5% of the anthropogenic carbon emissions, despite an unsettlingly high carbon footprint linked to cement production.[38–40] Carbonation of C-S-H is also of prime importance for the well-bore integrity[41–43] and valorization of construction and demolition wastes that places tangible pathways for net zero or even negative carbon footprint concrete technologies within reach[44]. The motivation to conduct a comparative study between C-S-H and forsterite is two-fold and goes far beyond their technological significance. First, while forsterite is a natural mineral dominated by macroscopic fracture networks, C-S-H provides a nanoporous model system[45] that readily lends itself to studies of confined fluids[46]. Second, the residence time of water in the first hydration shell of $Mg^{2+}$ cations is at least three orders of magnitude longer than that around $Ca^{2+}$ ions.[47] Such extended residence time can potentially hinder dehydration processes and regulate interfacial processes in rock-water-$CO_2$ systems.[48]

Herein, we employ molecular simulations to determine competitive sorption of $CO_2$ and $H_2O$ in metal silicate nanopores and address two basic questions surrounding the interactions of humidified $CO_2$ with forsterite and C-S-H within the thermodynamic range of technological interest. First, we seek to quantify the impact of nanoporosity and chemical composition on the thickness of interfacial adsorbed water films. While molecular simulations delineate the structure

and energetics of single- and multi-component fluids on metal silicate surfaces[49–51], quantitative measurements of the adsorbed water film thickness and its dependence on thermodynamic state variables of $CO_2$-$H_2O$ mixture (pressure, temperature), surface chemistry and pore size remain to be understood. These gaps are difficult to address experimentally and are key for parameterizing realistic MD simulations of these interfaces[49,52–54]. Although continual progress is being made in determining water film thicknesses at mineral-$H_2O$-$CO_2$ interfaces[54–64], including for forsterite surfaces, the initial hydration state of the mineral surface to measurements is often unknown, and the influence of pressure-temperature-composition on water film thicknesses has not been systematically explored. Second, we investigate whether carbonic acid and bicarbonate can potentially form at the water-solid interface. To this end, we determine the energetic penalty for displacing $CO_2$ through interfacial water layers toward the surface and model its subsequent reaction with hydroxyl groups and adsorbed water molecules.

## Results and Discussion:

**Formation of interfacial water films on metal silicate surfaces in contact with wet $CO_2$-rich fluids:** When the $CO_2$-$H_2O$ mixture invades the pore structure of the host rock ($Me^{2+}$ silicates), the $CO_2$-$H_2O$ molar fraction changes according to the surface chemistry and the confinement geometry. Therefore, for water-bearing $CO_2$ sequestration applications where carbonation reactions occur at the confined thin water film on the $Me^{2+}$ silicates, it is critical to understand the molar fractions of water (adsorbed water film thickness) and $CO_2$ that exist in the pore.

To unravel the $CO_2$-$H_2O$ mixture composition in the slit-pore, we perform Grand Canonical Monte Carlo (GCMC) simulations of competitive $CO_2$-$H_2O$ adsorption. Unlike the classical molecular dynamic (MD) that keeps the number of atoms and molecules fixed during the simulation, GCMC allows the exchange of species between a pre-defined reservoir and the simulation box making it the proper computational platform to model adsorption phenomena. We perform GCMC calculations with four types of wet $CO_2$-rich fluids on the surface of defective Hamid tobermorite[65] ($Ca_{2.25}[Si_3O_{7.5}(OH)_{1.5}]\bullet 1H_2O$)) (001) at 1.7 Ca/Si ratio as an analog of C-S-H[35] and hydroxylated (010) surface of forsterite. In GCMC simulations, one fluid corresponds to the normal carbonation at ambient conditions, two are relevant to water-bearing supercritical $CO_2$ fluids at geological conditions[3], and one relates to an intermediate gaseous $CO_2$. For thermodynamic conditions

**Table 1.** Thermodynamic properties of $H_2O$-$CO_2$ bulk mixtures in ambient condition, gaseous (g), and supercritical (sc) conditions.

| | T(K) | P(bar) | $\mu_{H_2O}(\frac{kJ}{mol})$ | $\mu_{CO_2}(\frac{kJ}{mol})$ | $\rho^{CO_2-rich}$ (g/cm$^3$) | $x_{CO_2}^{CO_2-rich}$ Mole Fraction |
|---|---|---|---|---|---|---|
| Ambient Condition | 300 | 1 | -46.00 | -40.00 | 0.0002 | 0.9756 |
| $CO_2$(g) at 20 bar | 300 | 20 | -46.00 | -33.25 | 0.0409 | 0.9982 |
| sc$CO_2$ at 100 bar | 348.15 | 100 | -47.00 | -35.75 | 0.2125 | 0.9942 |
| sc$CO_2$ at 200 bar | 348.15 | 200 | -47.00 | -34.50 | 0.5965 | 0.9956 |

corresponding to the above-mentioned four fluid mixtures, see **Table 1, Supplementary Note 1,** and **Supplementary Figs. S1-S3**. The relative humidity across these conditions is roughly 90%.

The slit pore in C-S-H is varied between 26 Å to 54 Å to explore its nanoporous structure. The forsterite simulations are focused on a 44 Å slit pore, which represents a cleaved surface and proves large enough to prevent imbibition. These olivine nanopores, including grain boundaries and fluid inclusions, are important dynamic environments that host dissolution-precipitation and mass transfer reactions that promote volume changes and reactive cracking.[66–69] More generally, these reactive nanopores are important in mafic rocks, including basalts, as Luhmann et al.[70] (ultra)small-angle neutron scattering measurements showed that CO2-rich brine increases the basalt's porosity, leading to pore sizes in the range of ~1 nm to 1 μm in response to secondary reactions and shrinkage-induced volume changes.

As presented in **Fig. 1.a-h**, interfacial water films persist on metal silicate surfaces even at supercritical $CO_2$ conditions and shield surfaces from direct contact with the segregated $CO_2$-rich phase. Similar observations are also reported for clays[50] and calcite[71,72], which suggest nanometer-thick water films should prevail on hydrophilic mineral surfaces when put in contact with a humidified $CO_2$-rich fluids. Interestingly, for the case of $scCO_2$ at 100 bar and 348 K, imbibition occurs in the slit-pore of C-S-H with a size as large as 44 Å, see **Fig. 1.b**. However, when we increase the $CO_2$ pressure to 200 bar, $CO_2$ manages to enter the same slit-pore size, as shown **Fig. 1.a**. On the other hand, water is only present as layers on the C-S-H surfaces at ambient (1 bar) and 20 bar $CO_2$(g) at 300 K (**Fig. 1.c and Fig. 1.d**).These two observations show the critical role of pressure and temperature in diffusion-to-imbibition transition at undersaturated water vapor

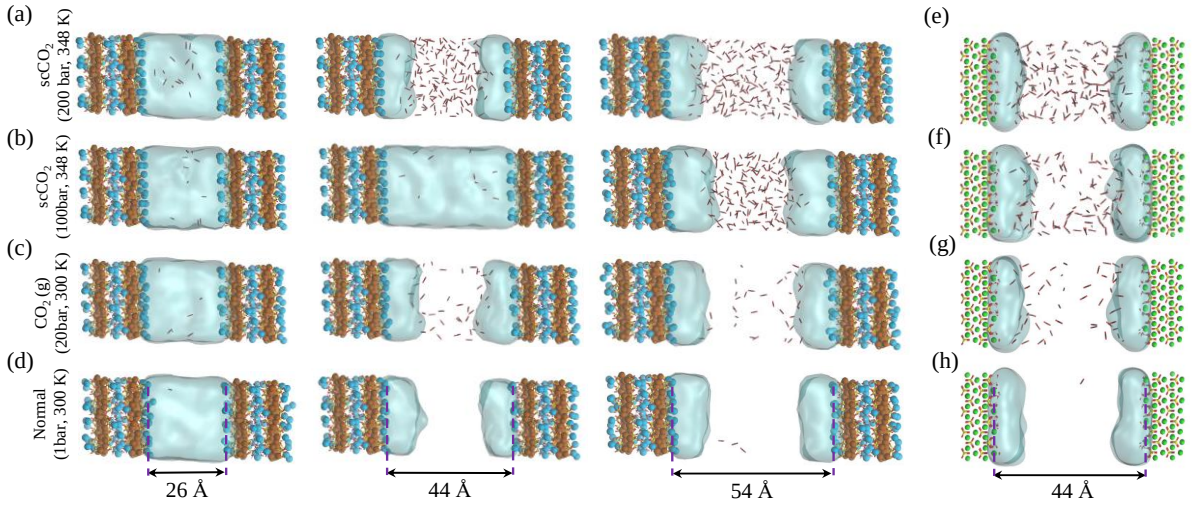


**Figure 1.** Competitive adsorption of $H_2O$-$CO_2$ mixtures in the slit C-S-H and forsterite porosity at normal, gaseous, and supercritical conditions. (a-d) Snapshots from the equilibrated two-phase GCMC adsorption simulations in C-S-H slit pores at different pore sizes and thermodynamic conditions. (e-h) Snapshots from equilibrated two-phase GCMC adsorption simulations in forsterite slit pores at different thermodynamic conditions. Blue and brown spheres represent intralayer and interlayer calcium in C-S-H, respectively. Green sphere represents magnesium. Silicate chains are depicted in yellow-red sticks. The continuous light blue cloud represents water and $CO_2$ is shown by black and red sticks.

pressure. Also, in contrast to C-S-H, we observe that $CO_2$ permeates into the slit-pore of forsterite at the $CO_2$ pressure of 100 bar and temperature of 348 K, as shown in **Fig. 1.f**. This emphasizes the role of surface chemistry in the fluid phase behavior in confined spaces, and it is a signature of the more hydrophilic surface of C-S-H than the {010} surface of forsterite.

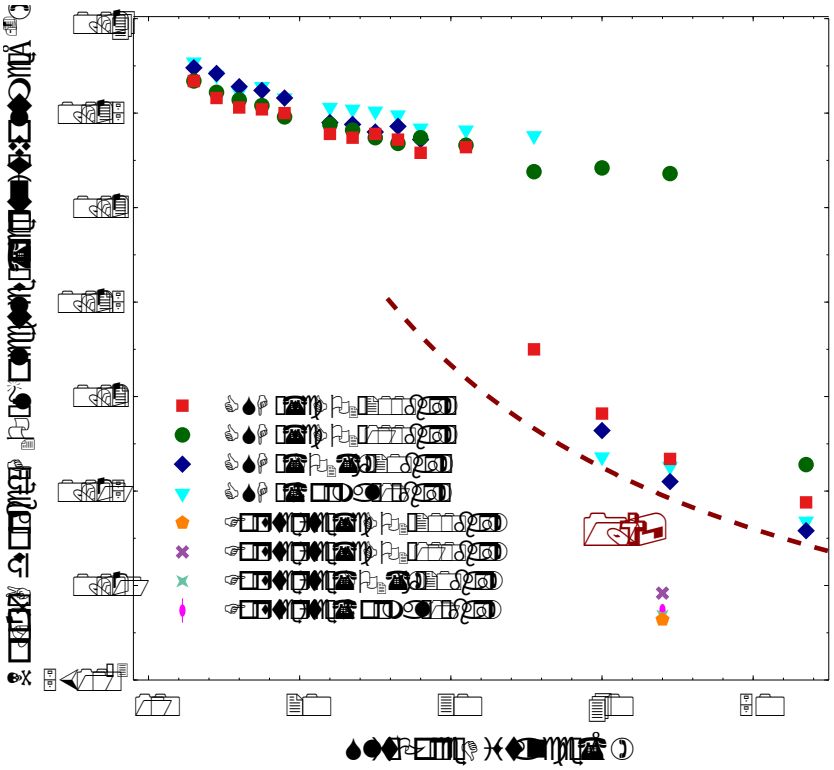

**Figure 2.** Number of adsorbed $H_2O$ molecules per unit volume based on the slit-pore distance. 1/V dashed line shows that the number of adsorbed water molecules is constant beyond a certain slit pore.

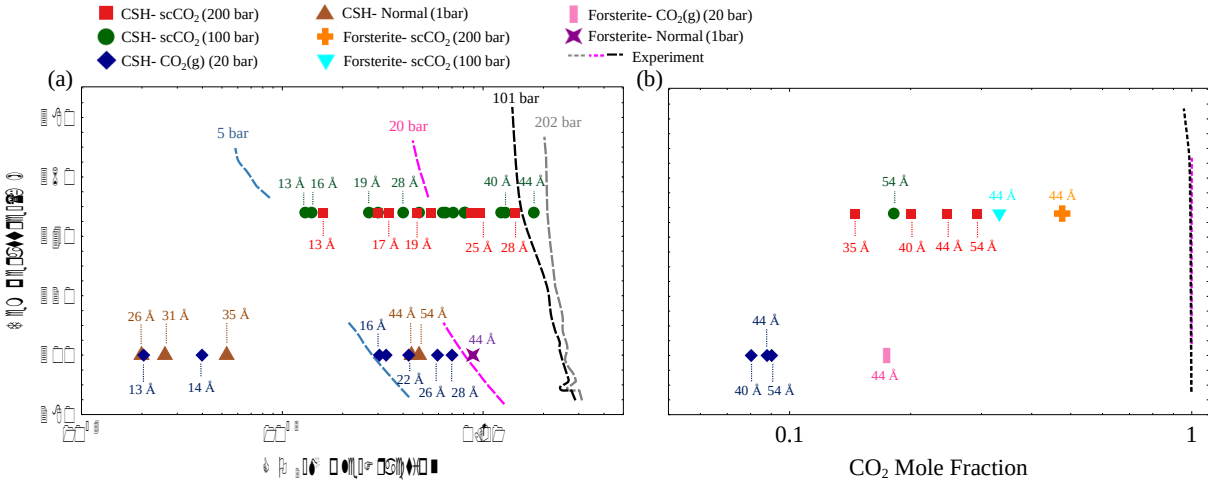


**Figure 3.** The $H_2O$-$CO_2$ phase coexistence diagram overlaid with the adsorbed mixture composition in the slit nano-porosities under various thermodynamic conditions computed via GCMC simulations. Dashed lines represent experimental and theoretical curves for the bulk mixture[70,71]. (a) Phase diagrams for $H_2O$-rich water-$CO_2$ mixtures. (b) $CO_2$-rich water-$CO_2$ mixtures. The $CO_2$ mole fractions in the slit-pore of C-S-H and forsterite derived from GCMC simulations are consistently lower than their bulk counterparts.

In the temperature and pressure ranges considered here, $CO_2$ could only penetrate the slit pore when the interlayer distance is more than 30 Å, while the interfacial water remains on the surface regardless of the distance, **Fig. 2**. Moreover, the total number of adsorbed water molecules converges to an asymptotic value at large pore sizes (> 40 Å), as shown by the dashed line in **Fig. 2**. The number of adsorbed water molecules per volume on the surface of forsterite is in general lower than that on the surface of C-S-H, again showing the more hydrophilic surface of C-S-H than forsterite. Also, at the largest slit-pore distance (54 Å for C-S-H and 44 Å for forsterite), we observe that the number of adsorbed water molecules on the surface of forsterite/C-S-H at 200 bar and 348K is lower compared to those at 100 bar and 348K. Similar observations can be made for simulations at 300K, and therefore we can conclude that $CO_2$ pressure can affect the amount of water adsorbed on the surface. It is also noteworthy that at interlayer distances of less 20 Å, the density of capillary water is found to be higher than its bulk value (1 g/cm$^3$) consistent with the simulations on the confined nature of water in C-S-H[73,74], see **Supplementary Fig. S4**.

To gain a more quantitative picture of the phase behavior, the resultant $CO_2$ mole fractions are overlaid on the experimental and theoretical bulk mixture phase diagram[75,76] in **Fig. 3**. The $CO_2$ molar fractions corresponding to $H_2O$-rich and $CO_2$-rich are respectively shown in **Fig. 3.a** and **Fig. 3.b**. Here, we show that the $CO_2$ mole fraction in the slit-pore of C-S-H and forsterite with the size of less than 5nm deviates from its bulk counterpart denoted by dashed lines in **Fig. 3.a** and **Fig. 3.b**. Also, although all GCMC simulations are initialized at $CO_2$-rich conditions, the equilibrium nanoconfined fluid in pores smaller than ~30 Å turns $H_2O$-rich, as shown in **Fig. 3.a**. The exact slit pore size at which $CO_2$-rich fluid shifts to $H_2O$-rich fluid depends on $CO_2$ pressure, temperature, and surface chemistry, among others. The observed deviation of $CO_2$ mole fraction from bulk values and the transition from $CO_2$-rich to $H_2O$-rich fluid in the confined space can be related to the hydrophilic nature of forsterite[49] and C-S-H[46] surfaces and the effect of surface forces in nanoscale confinements on the fluid phase behavior[26,27]. Beyond 30 Å, $CO_2$ permeates within the slit pores, and the mixture composition shifts toward the bulk $CO_2$-rich mixture (akin to the wet $CO_2$-rich reservoirs), as shown in **Fig. 3.b**. The observed confinement effect has implications, especially for multi-scale porous rocks such as C-S-H, which should be taken into account in continuum models and pore-scale models[77–79].

**Table 2.** The thickness of adsorbed water film on forsterite and C-S-H calculated via GCMC simulations and experiments.

| Forsterite Study | Experiment/Simulation | Pressure (bar) | Temperature (K) | Relative Humidity (%) | Reported Water Film Thickness on Forsterite (nm) |
|---|---|---|---|---|---|
| Loring et al. (2011) | Exp_1 | 182 | 323 | 136 | 2 [a] |
| Loring et al. (2011) | Exp_2 | 182 | 323 | 95 | 1 [a] |
| Loring et al. (2011) | Exp_3 | 182 | 323 | 81 | 0.1 [a] |
| Thompson et al. (2014) | Exp_4 | 100 | 308 | 93 | 1.9 [a] |
| Loring et al. (2015) | Exp_5 | 90 | 323 | 77 | 1.48 [b] |
| Loring et al. (2018) | Exp_6 | 90 | 323 | 77 | 1.71 [b] |
| Miller et al. (2019) | Exp_7 | 90 | 323 | 83 | 0.57 [b] |
| Miller et al. (2019) | Exp_8 | 90 | 323 | 84 | 0.66 [b] |
| Miller et al. (2019) | Exp_9 | 90 | 323 | 85 | 0.62 [b] |
| Miller et al. (2019) | Exp_10 | 90 | 323 | 83 | 0.57 [c] |
| Miller et al. (2019) | Exp_11 | 90 | 323 | 85 | 0.52 [c] |
| Placencia-Gómez et al. (2020) | Exp_12 | 90 | 323 | 85 | 1 [b] |
| Kerisit et al. (2021) | Exp_13 | 90 | 323 | 65 | 0.23 [b] |
| This Work | Sim_1 | 200 | 348 | 90 | 0.7 [d] |
| This Work | Sim_2 | 100 | 348 | 90 | 0.8 [d] |
| This Work | Sim_3 | 20 | 300 | 90 | 0.6 [d] |
| This Work | Sim_4 | 1 | 300 | 90 | 0.8 [d] |
| C-S-H Study | Experiment/Simulation | Pressure (bar) | Temperature (K) | Relative Humidity (%) | Reported Water Film Thickness on C-S-H Surface (nm) |
| This Work | Sim_5 | 200 | 348 | 90 | 1.3 [d] |
| This Work | Sim_6 | 100 | 348 | 90 | 1.4 [d] |
| This Work | Sim_7 | 20 | 300 | 90 | 1.25 [d] |
| This Work | Sim_8 | 1 | 300 | 90 | 1.25 [d] |

[a] Molar concentration of water determined using Beer's law in FTIR setup
[b] Measured by IR titration using $H_2O$
[c] Measured by IR titration using $D_2O$
[d] Calculated in this work via Grand Canonical Monte Carlo simulations

Determining the thickness of the adsorbed water film on the surface of metal silicate minerals is critical as it is a first-order control for carbon mineralization rates and mechanisms but is difficult to probe experimentally. **Table 2** is a compilation of water film thickness data from several experiments along with our adsorption simulation results. As shown in this table, experiments and simulations show adsorbed water film with thicknesses in the nano-meter range. According to our GCMC adsorption simulations, the average water film thickness on the forsterite surface is in the range of 0.6-0.8 nm depending on the temperature and pressure of the simulation. They are in good agreement with experimental values, especially those reported in recent years such as Exp_7,

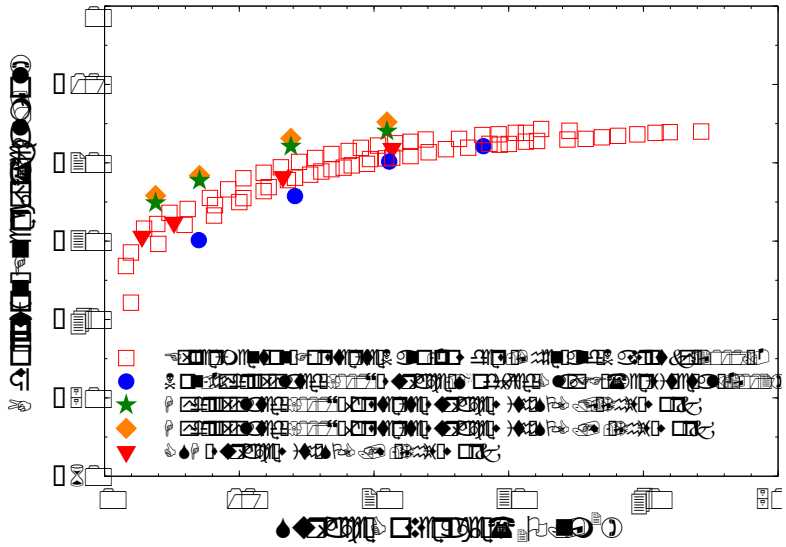

**Figure 4.** The calculated water adsorption energies on C-S-H and forsterite surfaces. Calorimetry measurements[76] and previous classical MD simulation results[44] on non-hydroxylated surface of forsterite are also presented for comparison.

Exp_8, Exp_9, and Exp_12 in **Table 2**. Nevertheless, we observe slight variability for the average film thickness on the surface at different carbonation conditions. To address the variability of water film thickness based on $CO_2$ pressure, a better picture could be achieved by calculating the distribution of species at variable carbonation conditions.

The water film thickness on the surface of C-S-H is shown to be higher than that on the hydroxylated surface of forsterite, as shown in Table 2. To clarify latter point, we calculate the water adsorption energies for different number of water monolayers on both surfaces. The water adsorption energies for 1, 2, 3 and 4 monolayers of water on the {010} hydroxylated surface of forsterite and C-S-H are shown in **Fig. 4**. The water adsorption energies on the surface of C-S-H are shown to be consistently lower than that of hydroxylated surface of forsterite. B3LYP calculations on gas phase clusters[80] show that hydration energies of $Mg^{2+}$ cation are in general lower than that of $Ca^{2+}$. However, AIMD simulations[52] show that calcio-olivine ($\gamma$-$Ca_2SiO_4$), a crystalline calcium silicate structure, are more hydrophilic than forsterite when ½ monolayer to 2 monolayers water are adsorbed on the surface. C-S-H is more disordered and has more defects than calcio-olivine, which could entail even higher affinity to water.

For comparison, the adsorption energies derived from calorimetry measurments[81] and previous MD simulations on the non-hydroxylated {010} surface of forsterite[49] are also included in **Fig. 4**.

Our calculations overestimate the adsorption energies on the hydroxylated surface of forsterite by about 2-3 kcal/mol compared to the upper values of calorimetry experiments. This slight discrepancy could be potentially due to the forcefield artifacts, or an indication that not all silicate groups dissociate water molecules adjacent to the surface. We should also emphasize that, using the same forcefield, Kerisit et al.[49] derive a lower adsorption energy for associative adsorption of a single water monolayer on the non-hydroxylated surface of forsterite compared to experiments.

We also note that the water surface coverage for the first monolayer of hydroxylated forsterite and C-S-H are lower than that on the non-hydroxylated forsterite surface, **Fig. 4**. We can attribute this to the surface structure of these solids where dissociated water molecules are initially added to the surface resulting in the hydration of silicate groups and the presence of hydroxyl groups adjacent to metal cations. Therefore, the water surface coverage in hydroxylated structures with two monolayers is equivalent to one monolayer on the non-hydroxylated surface.

In addition, we calculate the adsorption energies of forsterite surface with SPC/Fw water model[82], which is a modification of SPC model with flexible bonds and angle, compared to SPC/E water model that was originally incorporated in the modified ClayFF[49] for the surface of forsterite. As pointed out in the methods section, our GCMC calculations are performed with SPC water model which has different oxygen and hydrogen charges than SPC/E, and therefore a different dipole moment. We use SPC model in our GCMC calculations because it predicts the vapor pressure of water more accurately than SPC/E[83]. Nevertheless, upon our calculation of water adsorption energies on the surface forsterite, SPC/Fw water model only slightly overestimates the adsorption energies compared to SPC/E model, as shown in **Fig. 4**.

To resolve the spatial distribution of $CO_2$ and $H_2O$ molecules as well as surface hydroxyl groups in the slit pore, we perform MD on fully equilibrated confined GCMC simulations. The details of these simulations are presented in the Methods section. The quantitative spatial distribution of water, $CO_2$, and hydroxyl groups are presented in **Fig. 5**. The formation of nanometer-thick interfacial water layers is evident from distributions, acting as a barrier for $CO_2$ molecules to directly contact the surface. Regardless of thermodynamic conditions, we observe four peaks in the water number density distributions on the surface of forsterite, see **Fig. 5.a-d**. However, the furthest peak from the surface does not represent a fully formed water layer. This is consistent with a recent $scCO_2$-forsterite experiments[61], which shows 3.5 water monolayers form on the forsterite surface at 85% relative humidity. On the other hand, we also observe water layers formed on the surface of C-S-H at all pore sizes, see **Fig. 5.e-h**. However, due to the appearance of multiple peaks close to each other, it is hard to distinguish water monolayers, although the overall water film thickness on C-S-H is higher than that on forsterites. These irregularities of the water density peaks on the surface of C-S-H could partly result from the observation that surface calcium atoms are more labile and less attached to the surface compared to surface magnesium on forsterite. This enables the water molecules to penetrate inside the C-S-H gel and attach to the second calcium layer and silicate groups, as shown in **Fig. 5. e-h**. Another reason for this irregularity on the C-S-H surface is a more disordered layering of calcium ions that attract water molecules, and the defects

and nanoscale cavities resulting from defective silicate chains. Therefore, hydrogen bonds form between water molecules, hydroxides, and hydrated silicates that are scattered at different elevations from the surface. The heterogeneity of hydrogen bonds in the disordered C-S-H structure is studied before through both simulations and experiments.[73,74,84,85]

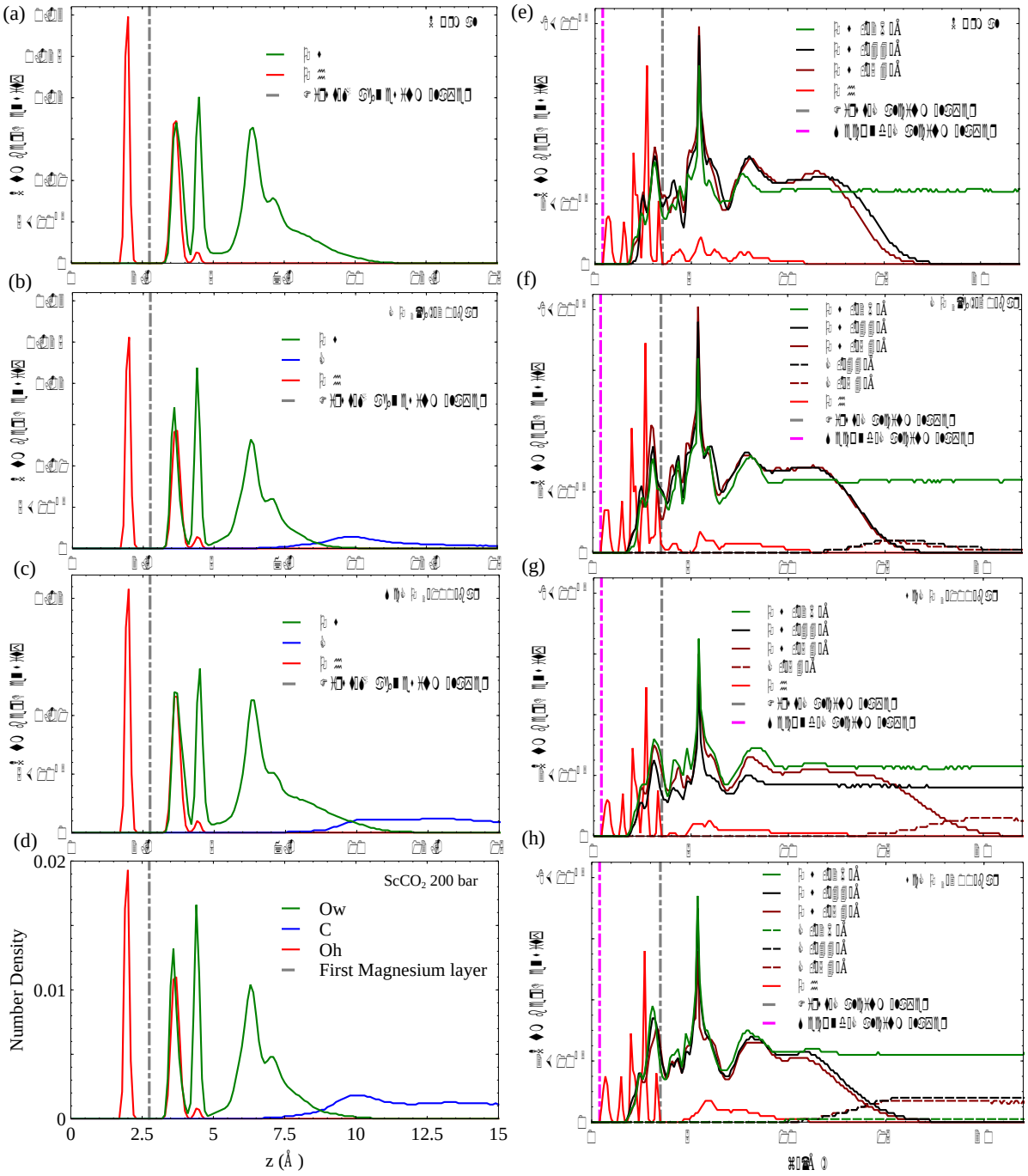


**Figure 5.** The average distribution of $H_2O$, $CO_2$, and OH- species in the slit-pore of forsterite and C-S-H. (a-d) Distribution of species in the slit-pore of forsterite at normal, $CO_2$ (g), $scCO_2$ (100 bar), $scCO_2$ (200 bar), respectively. (e-h) Distribution of species in the slit-pore of C-S-H at normal, $sbCO_2$, $scCO_2$ (100 bar), $scCO_2$ (200 bar), respectively. The average location of the first magnesium layer on the surface of forsterite, as well as the location of the first and second calcium layers on C-S-H surface are shown by vertical dashed lines. Ow, C, and Oh represent water oxygen, carbon in carbon dioxide, and surface hydroxide oxygen, respectively.

The formation of hydration layers has been previously reported for both forsterite[49] and C-S-H[51] in unsaturated and saturated conditions, respectively. Additionally, recent Fast Force Mapping (FFM) experiments on the surface of bohemite[86] illustrates the formation of first water layer on the surface cavities (here, the silicate groups), and the second layer forming on top of hydroxide groups. This is consistent with our results on the surface of forsterite as shown in **Fig. 5. a-d**. For the surface of C-S-H, which is much more disordered, the appearance of multiple water density peaks around the surface demonstrates the same phenomena, as shown in **Fig. 5. e-h.**

Another significant aspect of the distribution diagrams is that upon the entrance of the dense $CO_2$ inside the pore, the last water layer contracts and $CO_2$ distribution peaks at the interface, as could be seen by comparing the distribution at ambient (1 bar) gaseous to supercritical $CO_2$ (100, 200 bar) in **Fig. 5**. Although, the number of water layers do not change, this could be a sign that $CO_2$ pressure, if above a certain threshold, might alter the number of water layers. The appearance of interfacial peaks in $CO_2$ distribution at all four conditions is a characteristic of immiscible mixtures verified through both experiments and simulations.[87–90] However, after juxtaposing water distributions with those of carbon dioxide, we confirm that although $CO_2$ is not a good solvent for dipolar water, the appearance of overlapping shoulders between two species is indicative of enhanced mutual solubility at the interface. This is attributed to the interfacial capillary wave phenomenon and the Coulombic attraction between $H_2O$ and $CO_2$ molecules.[20] This could potentially amplify the rate of $CO_2$ speciation at the interface. Another important feature of the resulted distributions is that the proximity of $CO_2$ and hydroxides within the nanolayered hydration films, especially on the surface of C-S-H, may increase the rate of bicarbonate and carbonate production. Although it is well established from previous simulations that the thin water film on hydrophilic material displaces $CO_2$ away from the surface, this proximity of $CO_2$ molecules and surface hydroxides motivates us to next explore the energetics of $CO_2$ physisorption on the surface.

**Energetics of $CO_2$ speciation on metal silicate surfaces:** Our adsorption simulations are non-reactive in essence. Thus, it is critical to resolve the mechanistic picture of $CO_2$ speciation in adsorbed water nanofilms. It is possible that $CO_2$ speciates to carbonic acid and bicarbonate within the nanofilm in the presence of dissolved cations.[61] Moreover, it is probable that $CO_2$ reacts with surface hydroxyl groups and surface cations. However, since $CO_2$ molecules are displaced from the surface due to the presence of the adsorbed water film, it is necessary to quantify the free energy required to bring $CO_2$ close to the surface. Since the residence time of water molecules around solvated $Mg^{2+}$ ion is in the order of microseconds[47], the water coordination number around surface $Mg^{2+}$ cations is important. Therefore, to sample the full phase space in our free energy calculation for the adsorption of $CO_2$ on forsterite surface, we consider the surface Mg water coordination number in addition to the perpendicular distance of $CO_2$ from the surface. The coordination number is defined as:

$$CN = \sum_{i \in \{Ow\}} \frac{1-\left(\frac{r_i - d_0}{r_0}\right)^n}{1-\left(\frac{r_i - d_0}{r_0}\right)^m} \quad (1)$$

where $r_{ij}$ is the distance of water molecule *i* with the surface Mg, $r_0$ is set to 1 Å, $d_0$ is set to 2.2 Å, *n* is equal to 4, and *m* is equal to 8. The value of $d_0$ is taken from the peak distance of the surface Mg-water pair distribution function.

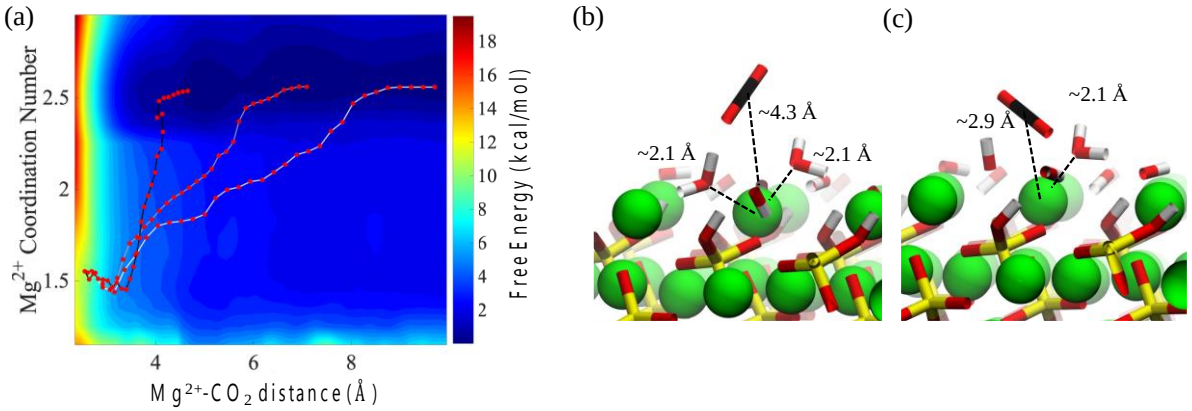


**Figure 6.** Potential-of-Mean-Force (PMF) for the adsorption of $CO_2$ from the solution on the surface of Forsterite. (a) 2D PMF for the adsorption $CO_2$ on the surface. The three red-dotted paths represent minimum free energy paths corresponding to $CO_2$ adsorption from the edge of the 2nd, 3rd and 4th adsorbed water layer. While these three paths are distinct, they show that $Mg^{2+}$ dehydration is necessary for the adsorption of $CO_2$ on the forsterite surfaces. Surface magnesium and the adsorbed $CO_2$ molecule with (b) two and (c) one neighboring water molecule. Free energy calculations show the departure of one water molecule is thermodynamically necessary for $CO_2$ adsorption.

The resulting two-dimensional free energy landscape is shown in **Fig. 6. a.** The minimum energy path (MEP) of the $CO_2$ molecule as it goes from the solution to the vicinity of the surface is calculated via the Nudged Elastic Band technique (NEB) method[91]. As shown in the figure, the coordination number of surface Mg changes from two to one as $CO_2$ is approaching the surface. Also, depending on the initial location of the $CO_2$ molecule, three distinct MEPs are derived for the cases where $CO_2$ is initially located at the 2nd, 3rd, and 4th layers of the adsorbed water, as shown in **Fig. 6. a.** However, the energy that is required for the $CO_2$ molecule to pass through the layers and reach the surface is not affected by the initial position of the $CO_2$. This perhaps shows that regardless of the number of adsorbed water layers, which depends on the relative humidity and $CO_2$ pressure, the energy of $CO_2$ physisorption on the forsterite surface is unique. Also, the calculated free energy of $CO_2$ adsorption is 2.5 kcal/mol higher than the adsorption free energy previously calculated by Kerisit et al.[49] for the non-hydroxylated {010} surface of forsterite. However, the magnesium coordination number was not considered in the PMF calculation in that work. Therefore, this energy difference could either be the consequence of incorporating magnesium coordination number, the existence of a stronger hydrogen bond structure due to surface hydroxides, or the difference in computational methods used.

It is noteworthy that although we calculate the free energy of $CO_2$ adsorption on the surface in contact with bulk water, it was previously shown that the structure of the water layers is not drastically different when the forsterite surface is in contact with various number of water

monolayers and supercritical $CO_2$.[49] These findings are consistent with *in situ* XRD measurements of $H_2O$-$CO_2$ sorption in hydrophilic montmorillonite[92,93], where $CO_2$ intercalation was found limited when the hydration level goes beyond one water layer, regardless of isomorphous $Me^{2+}$ exchange.

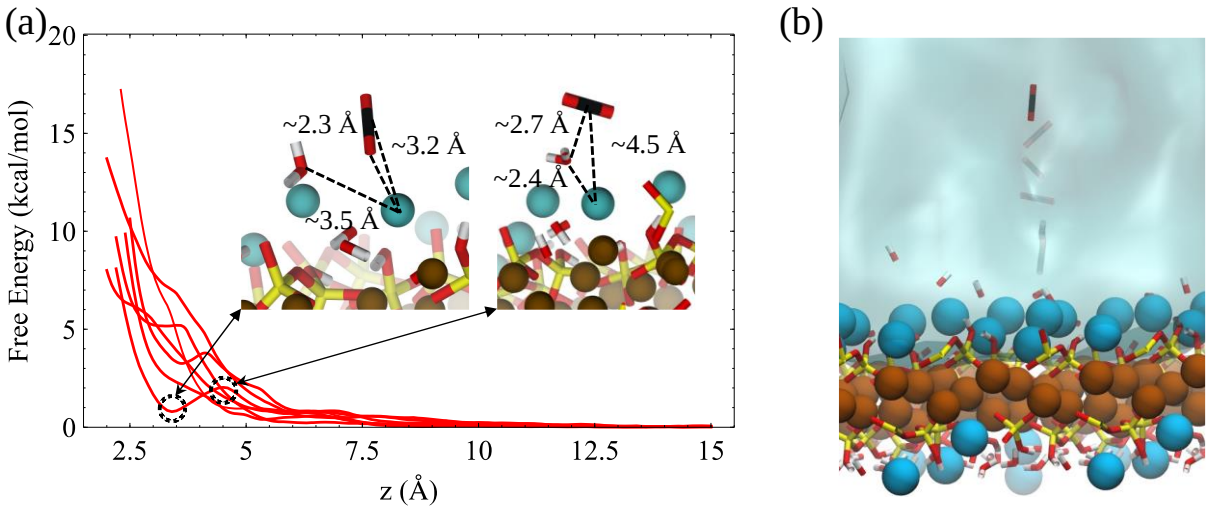


**Figure 7.** Non-reactive interaction of $CO_2$ molecule with wet C-S-H. (a) Physisorption of a $CO_2$ molecule on the surface of C-S-H. Multiple free energy curves are derived for random surface calcium atoms. The insets demonstrate a $CO_2$ molecule on the surface at the metastable state and the transition state. (b) The umbrella sampling stages for the adsorption of $CO_2$ on the surface.

We also calculate the associative adsorption of $CO_2$ at random surface sites of C-S-H, as shown in **Fig. 7**. We find that, like the forsterite case, $CO_2$ is more stable in the solution than adsorbed in the on the surface. However, a metastable state is observed when the $CO_2$ molecule and surface $Ca^{2+}$ ions are separated by about 3.2 Å on the C-S-H surface. As shown in the inset, the oxygen of the $CO_2$ molecule in the metastable state is oriented toward the surface calcium cation, reminiscent of a weakly chemisorbed state[94]. Unlike the forsterite case where no minimum is observed, this unique characteristic of the C-S-H surface urges us to consider interfacial $CO_2$ reactions.

For the carbonation progression, the physisorbed $CO_2$ must speciate to carbonic acid and bicarbonate by reacting with interfacial water molecules or surface-bound hydroxide. Here, we use Density Functional Theory (DFT) along with the Nudged Elastic Band (NEB) method to calculate the corresponding reaction paths, see the Methods section. **Fig. 8. a** summarizes the three reaction paths. The adsorbed, transition, intermediate, and product states are schematically shown for each reaction path in **Fig. 8.b-e**.

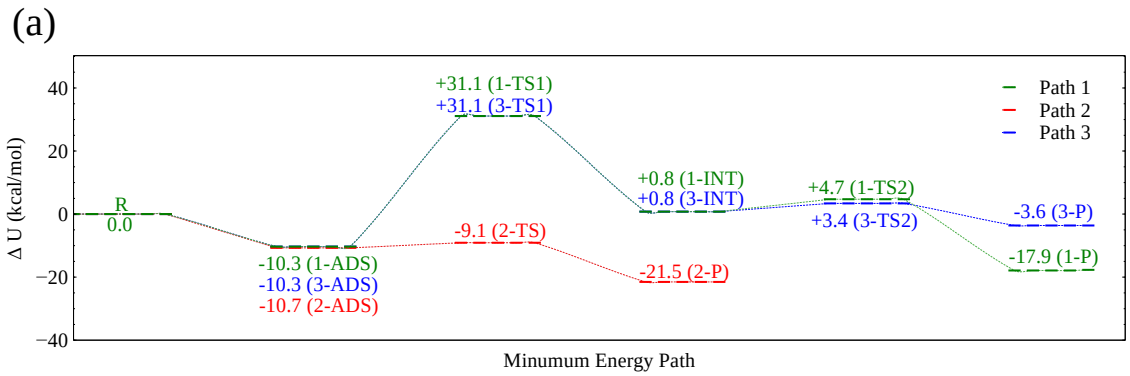
(a)
Δ U (kcal/mol)
Minumum Energy Path
R
0.0
-10.3 (1-ADS)
-10.3 (3-ADS)
-10.7 (2-ADS)
+31.1 (1-TS1)
+31.1 (3-TS1)
-9.1 (2-TS)
-21.5 (2-P)
+0.8 (1-INT)
+0.8 (3-INT)
+4.7 (1-TS2)
+3.4 (3-TS2)
-3.6 (3-P)
-17.9 (1-P)
Path 1
Path 2
Path 3

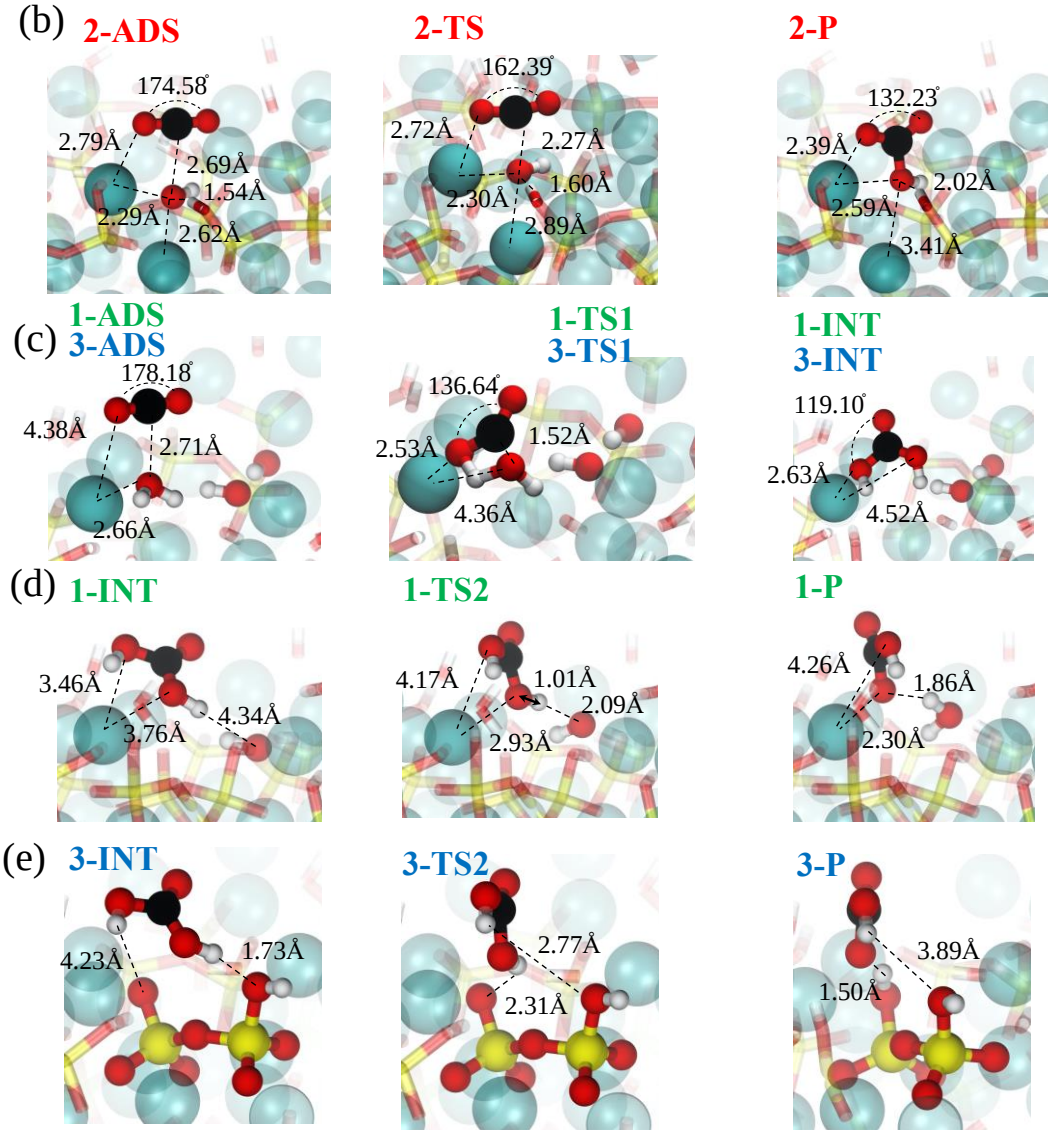
(b)
2-ADS
174.58°
2.79Å
2.69Å
1.54Å
2.29Å
2.62Å
2-TS
162.39°
2.72Å
2.27Å
1.60Å
2.30Å
2.89Å
2-P
132.23°
2.39Å
2.02Å
2.59Å
3.41Å
(c)
1-ADS
3-ADS
178.18°
4.38Å
2.71Å
2.66Å
1-TS1
3-TS1
136.64°
2.53Å
1.52Å
4.36Å
1-INT
3-INT
119.10°
2.63Å
4.52Å
(d)
1-INT
3.46Å
4.34Å
3.76Å
1-TS2
4.17Å
1.01Å
2.09Å
2.93Å
1-P
4.26Å
1.86Å
2.30Å
(e)
3-INT
4.23Å
1.73Å
3-TS2
2.77Å
2.31Å
3-P
3.89Å
1.50Å

**Figure 8.** Reactive interaction of $CO_2$ molecule with wet C-S-H. (a) DFT calculation of the reaction pathways between $CO_2$ and C-S-H. (Path 1) The reaction between $CO_2$ and bound water at the hydroxide site. (Path 2) The reaction between $CO_2$ and surface-bound hydroxide. Strong physisorption is followed by a chemical reaction with a low barrier leading to the formation of bicarbonate. (Path 3) The reaction between $CO_2$ and bound water at the dangling oxygen site. (b) Snapshots of the adsorbed state (ADS), transition state (TS) and product (P) for reaction paths 2. (c) Snapshots of the ADS, TS and intermediate (INT) state for the reaction of surface water and $CO_2$ in path 1 and 3. d) Snapshots of the dissociation of carbonic acid to bicarbonate through reaction with surface hydroxide. e) Snapshots of the dissociation of carbonic acid to bicarbonate through reaction with dangling oxygen in silicates.

The most significant reaction occurs at the hydroxide site (path 2), where strong physisorption is connected to a chemical reaction by a low barrier, leading to the formation of bicarbonate, see **Fig. 8. b**. In a fully hydrated environment, it takes about 3-10 kcal/mol to bring $CO_2$ to the hydroxide site on the surface of C-S-H, see **Fig. 7.a**. The overall energy barrier associated with this path is lower than or in the same range of the free energy barrier for bicarbonate formation in solutions as calculated via *ab initio* MD[95]. However, the abundance of hydroxide sites on the surface of C-S-H considerably impacts the overall rate of bicarbonate formation when compared to solution reactions. On the other hand, the reaction barrier of $CO_2$ with water, according to paths 2 and 3, if seen from the adsorbate, is approximately 10 kcal/mol lower than the corresponding gas-phase reaction[96,97]. The snapshots of this reaction are shown in **Fig. 8. c**. Although our DFT simulations do not explicitly consider interfacial water molecules, these remarks clearly indicate the catalytic role of C-S-H surface. Furthermore, it should be noted that the addition of liquid water would further lower the barrier down to 19 kcal/mol, according to coupled-cluster theory CCSD(T) calculations [96], without taking to account any surface catalytic effects. Once carbonic acid forms, it can dissociate, either transferring a proton to a neighboring unhydrated dangling silicate dimer oxygen on the C-S-H surface (path 3), or a neighboring hydroxide (path 1), see **Fig. 8.d** and **Fig. 8.e**. With a wetted surface, the first option for proton transfer is unlikely, and the proton transfer to hydroxide is by far more exothermic. In both paths 1 and 3, the adsorbed $CO_2$ reacts with surface water and forms carbonic acid in a concerted reaction.

It is noteworthy that *ab initio* molecular dynamics (AIMD) simulations in the bulk aqueous water show that $CO_2$ could react with water to form bicarbonate and a hydronium ion, followed by the formation of carbonic acid in a stepwise reaction.[98] Similar route for this reaction could be imagined to happen in the adsorbed water nanofilm on C-S-H and forsterite leading to the formation of bicarbonate followed by the structural migration of excess proton to the surface hydroxide. Whether through reaction path 2 or in the adsorbed water nanofilm, the formation of bicarbonate is confirmed experimentally through *in situ* $^{1}H–^{13}C$ Cross-Polarized NMR spectroscopy on forsterite nanoparticles[61]. However, bicarbonates were not found on fused silica surfaces. As we demonstrated earlier in this work, it is energetically unlikely to bring $CO_2$ to the surface of forsterite in the presence surface water layers. Therefore, by ruling out the formation of

carbonic acid through direct reaction of $CO_2$ with the surface hydroxide or surface water, there remains two possible reaction pathways: The reaction of $CO_2$ with water 1) in the solvation shell of dissolved magnesium in the thin water film[61], or 2) at the interface of dense $CO_2$ and water nanofilm. However, for the further progression of carbonation reaction to carbonate nucleation whether on the C-S-H or forsterite, the carbonic acid needs to turn into bicarbonate and carbonate. The specific mechanisms for these deprotonation reactions are still not clear. We delve into the mechanistic picture of these reactions in a future paper.

**Methods:**

**Grand Canonical Monte Carlo Simulations.** Two-phase adsorption simulations in the present study, namely bulk mixture, and slit pore adsorption studies were carried out using the Grand Canonical Monte Carlo (GCMC) simulation approach. Towhee package [99] was utilized to perform all the Monte Carlo simulations in the grand canonical ensemble ($\mu_{H_2O}\mu_{CO_2}VT$) using the Configurational Biased Monte Carlo (CBMC) technique.[100] The configurational-biased insertion or deletion or reinsertion probabilities are 0.25 and 0.125 for water and $CO_2$ respectively. The biased molecular translation probabilities are 0.75 and 0.375 for water and $CO_2$ with maximum displacement 0.5Å. The biased molecular rotation probability is 0.5 for all molecules with the maximum rotation of 0.05 rad. Details of the bulk mixture adsorption simulations are provided in **Supplementary Note 1** and **Supplementary Fig. S1-S3**. The confined $CO_2$-$H_2O$ adsorption simulations are carried out between two C-S-H and forsterite slabs with dimensions of 26 Å x 23 Å, and 26 Å x 26 Å, respectively. Due to high computational costs, layers are fixed in these simulations. Such an assumption has a negligible effect on the adsorption properties in non-swelling systems such as hardened concrete and igneous rocks. We used the conventional SPC water model[101], EPM2 $CO_2$ model[102], and Lorentz-Berthelot combination rule to model $CO_2$-$H_2O$ mixtures. We note that such a combination might slightly underestimate the interfacial tension between water and carbon dioxide[17]. However, this would not significantly alter the thickness of interfacial water films that are governed by the water-mineral interfacial tension. ClayFF[103] and its modified version[49] are used respectively to model C-S-H and forsterite surfaces. We apply Lorentz-Berthelot mixing rules to describe solid-fluid interactions. While the Lorentz-Berthelot mixing rule overestimates the single water adsorption energy on forsterite by ~10% ($\Delta E_{cal}$=-31 kcal/mol vs. $\Delta E_{LBmixing}$ =-34 kcal/mol), it matches the adsorption energy measured via calorimetry at three mono-layers water coverage.[49] Therefore, the mixing rule satisfactorily predicts adsorption properties at thermodynamic conditions relevant to this work (RH~90%). However, a reparameterization of the modified ClayFF potential would warrant a better match with experiments and DFT calculations at lower relative humidity levels (water coverage below two monolayers). In contrast to ClayFF, variable charges for the C-S-H constituents were employed, similar to the previous simulation work on C-S-H [104], to ensure charge-neutrality. Before GCMC calculations, C-S-H layers are relaxed in the MD simulations with the CSH-FF potential, a version of ClayFF tuned specifically to model C-S-H structures and reproduce its mechanical properties. Similarly, MD relaxation is done for the hydroxylated {010} surface of forsterite using the modified Clay-FF potential. Forsterite surface was terminated at M2 sites

recognized as the most stable termination through X-ray reflectivity[105], DFT[52], and molecular simulations[106,107]. MD simulations are done in the NVT ensemble using the Nosé-Hoover thermostat with a relaxation time of 100 steps and the timestep of 1 fs. The adsorption process in the slit pore was performed at four different thermodynamic conditions represented in **Table 1**. All confined GCMC simulations are equilibrated at least 25 million Monte Carlo (MC) steps. We continued slow converging simulations up to 60 million steps to ensure proper convergence.

**Molecular dynamics simulations.** MD simulations are performed in the canonical ensemble (NVT) with Nosé-Hoover thermostat and time step of 1 fs using LAMMPS software.[108] We use the same potentials as in GCMC calculations except for C-S-H, where flexible SPC water model[109] and flexible EPM2 model for $CO_2$ molecules[110] were used. Also, SPC/E water model was used for Forsterite consistent with Kerisit et al[49]. We allow the first two layers of the surface to vibrate freely and kept the rest of the atoms in the substrate fixed to reduce the computational cost and for to enable the inner layers as a bulk-like structure. The cell is equilibrated for 100 ps, and the distribution analysis is derived from a production phase of 10 ns.

**Potential-of-Mean-Force (PMF) Calculations.** The energetics of the physisorption and dissociation of respectively carbon dioxide and metal on the solid surface is determined via the umbrella sampling (US) technique as implemented in the "PLUMED 2.5" add-on package to LAMMPS[111]. Here, we use a biased harmonic spring with a stiffness of 200 kcal/mol$Å^{-2}$ and 120 kcal/mol$Å^{-2}$ between the object ($CO_2$ molecule for the case of adsorption, $Me^{2+}$ cation for the case of dissociation) and a reference $Me^{2+}$ atom on the surface respectively. The normal distance to the solid surface is taken as the "collective variable" and sampling windows are separated by 0.1 Å. CSH-FF[112] and a modified version of Clay-FF[52] were used as forcefields for the adsorption of $CO_2$ on the surface of CSH and Forsterite respectively. An additional collective variable namely the surface Mg water coordination number is also considered, as discussed in the main text. The harmonic spring with stiffness of 2000 kcal/mol is chosen for the coordination number. Histograms of the distribution of the collective variables were produced after 500 ps of equilibration phase, and another 1 ns of the production phase of MD runs at 300 K in the NVT ensemble. The substrate (except the first two layers) were fixed. A weak harmonic potential was also considered in the 'xy' plane (parallel to the surface) to keep the $CO_2$ molecule in the desired adsorption/desorption site, enclosed in a cylinder with the fixed reference atoms on its base. The free energy difference is then obtained via the weighted histogram analysis method (WHAM)[113].

**Density Functional Theory Calculations.** A double layer of C-S-H with cell lengths a x b x c = 26.54 Å x 24.44 Å x 18.20 Å and cell angle $\gamma$ = 82.5° and the other angles 90° has been created with Ca/Si ratio of 1.7 as described in ref [104]. For stabilization, two layers of water were added on the lower surface. A single $CO_2$ molecule was placed 10 Å above the unwetted surface to obtain a reference structure for unreacted $CO_2$. The entire structure was pre-optimized using ReaxFF[104] as implemented in LAMMPS. First, an MD was run with a 0.25 fs time step and a ramp brought up the temperature from 1 K to 298.15 K within 100 ps. Next, the MD was allowed to run for 500 ps before the ensemble was cooled down to 1 K within 500 ps. This yields a realistic initial guess

structure for DFT calculations, with all chemically reasonable re-combinations and dissociations of water molecules completed. To obtain starting structures for adsorption and chemically reacted products, the $CO_2$ molecule had been shifted 3 Å and 1 Å above each reactive site, respectively. Reactive sites were 1) water on the surface 2) hydroxide on the surface, 3) an unhydrated dangling oxygen in a silicate dimer. This setup had been proven reasonable in a previous investigation[114]. The starting structures were then also pre-optimized as described above.

For all DFT calculations, the program CP2K[115] has been used with a combined Gaussian and plane waves ansatz. A double-ζ polarized basis set optimized for condensed phase[116] was applied together with a cutoff value of 500 Ry for the plane waves basis and GTH pseudopotentials [117–119]. The Kohn-Sham equations were solved to an accuracy of $10^{-6}$ $E_h$ with the revised PBE[120,121] GGA functional and the D3 set of dispersion corrections[122]. Extensive benchmark calculations show that revised PBE GGA functional with D3 dispersion correction is among the top performers in GGA functionals[123,124]. The pre-optimized structures were fully optimized without any constraints and the resulting structures were interpolated for NEB calculations. First, the NEB was optimized within the D-NEB framework until a maximum error of 5 $mE_h/a_0$ in RMS gradients and $10^{-2}$ $a_0$ in RMS displacement had been achieved. Next, the band optimization continued using IT-NEB[126] for 10 steps before it switched to CI-NEB[127] until the final convergence of 0.5 $mE_h/a_0$ in RMS gradients and $10^{-3}$ $a_0$ in RMS displacements had been achieved, which corresponds to an accuracy of at least 1 kJ/mol. Minima were converged to at least 0.45 $mE_h/a_0$ maximum gradient and 0.003 $a_0$ maximum displacements. We note that the direct calculation of eigenvalues through the diagonalization of the Hessian matrix is imperative to confirm the transition state obtained vis the NEB method. In the case of NEB calculations in this work, the number of plane waves is very high in our DFT calculations to the level that the calculation of the Hessian matrix becomes impractical.

**Acknowledgments:**
This material is based on work supported by the U.S. Department of Energy (DOE), Office of Science, Office of Basic Energy Sciences (BES), Chemical Sciences, Geosciences, and Biosciences Division through its Geosciences program at the University of California Irvine through an Early Career award to MJAQ (DE-SC0022301) and at Pacific Northwest National Laboratory (PNNL). Any opinions, findings, conclusions, or recommendations expressed in this material are those of the authors and do not necessarily reflect those of the funding agency. We also thank Dr. Russell Detwiler for fruitful discussions.

## Competing interests:

The authors declare no competing interests.

**References:**

1 J. M. Matter and P. B. Kelemen, *Nat. Geosci.*, 2009, **2**, 837–841.
2 S. K. White, F. A. Spane, H. T. Schaef, Q. R. S. Miller, M. D. White, J. A. Horner and B. P. McGrail, *Environ. Sci. Technol.*, 2020, **54**, 14609–14616.
3 S. R. Gislason and E. H. Oelkers, *Science*, 2014, **344**, 373–374.
4 M. Fernández Bertos, S. J. R. Simons, C. D. Hills and P. J. Carey, *J. Hazard. Mater.*, 2004, **112**, 193–205.

5 B. P. McGrail, H. T. Schaef, A. M. Ho, Y.-J. Chien, J. J. Dooley and C. L. Davidson, *J. Geophys. Res. Solid Earth*, , DOI:10.1029/2005JB004169.
6 D. S. Goldberg, T. Takahashi and A. L. Slagle, *Proc. Natl. Acad. Sci.*, 2008, **105**, 9920–9925.
7 D. S. Goldberg, D. V. Kent and P. E. Olsen, *Proc. Natl. Acad. Sci.*, 2010, **107**, 1327–1332.
8 C. Marieni, T. J. Henstock and D. A. H. Teagle, *Geophys. Res. Lett.*, 2013, **40**, 6219–6224.
9 S. Ó. Snæbjörnsdóttir, F. Wiese, T. Fridriksson, H. Ármansson, G. M. Einarsson and S. R. Gislason, *Energy Procedia*, 2014, **63**, 4585–4600.
10 I. M. Power, J. McCutcheon, A. L. Harrison, S. A. Wilson, G. M. Dipple, S. Kelly, C. Southam and G. Southam, *Minerals*, 2014, **4**, 399–436.
11 S. A. Wilson, A. L. Harrison, G. M. Dipple, I. M. Power, S. L. L. Barker, K. Ulrich Mayer, S. J. Fallon, M. Raudsepp and G. Southam, *Int. J. Greenh. Gas Control*, 2014, **25**, 121–140.
12 D. N. Huntzinger, J. S. Gierke, L. L. Sutter, S. K. Kawatra and T. C. Eisele, *J. Hazard. Mater.*, 2009, **168**, 31–37.
13 J. K. Stolaroff, G. V. Lowry and D. W. Keith, *Energy Convers. Manag.*, 2005, **46**, 687–699.
14 G. Rim, N. Roy, D. Zhao, S. Kawashima, P. Stallworth, S. G. Greenbaum and A.-H. Alissa Park, *Faraday Discuss.*, 2021, **230**, 187–212.
15 W. K. O'Connor, D. C. Dahlin, G. E. Rush, C. L. Dahlin and W. K. Collins, *Min. Metall. Explor.*, 2002, **19**, 95–101.
16 E. National Academies of Sciences, *Negative Emissions Technologies and Reliable Sequestration: A Research Agenda*, 2018.
17 I. C. Bourg, L. E. Beckingham and D. J. DePaolo, *Environ. Sci. Technol.*, 2015, **49**, 10265–10284.
18 J. Alcalde, S. Flude, M. Wilkinson, G. Johnson, K. Edlmann, C. E. Bond, V. Scott, S. M. V. Gilfillan, X. Ogaya and R. S. Haszeldine, *Nat. Commun.*, 2018, **9**, 2201.
19 L. D. Gelb, K. E. Gubbins, R. Radhakrishnan and M. Sliwinska-Bartkowiak, *Rep. Prog. Phys.*, 1999, **62**, 1573–1659.
20 B. K. Peterson, J. P. R. B. Walton and K. E. Gubbins, *J. Chem. Soc. Faraday Trans. 2 Mol. Chem. Phys.*, 1986, **82**, 1789–1800.
21 E. E. Santiso, A. M. George, M. Sliwinska-bartkowiak, M. B. Nardelli and K. E. Gubbins, *Adsorption*, 2005, **1**, 349–354.
22 N. Chakraborty, Z. Karpyn, S. Liu, H. Yoon and T. Dewers, *J. Nat. Gas Sci. Eng.*, 2020, **76**, 103120.
23 A. Cihan, T. K. Tokunaga and J. T. Birkholzer, *Langmuir*, 2019, **35**, 9611–9621.
24 T. K. Tokunaga, W. Shen, J. Wan, Y. Kim, A. Cihan, Y. Zhang and S. Finsterle, *Water Resour. Res.*, 2017, **53**, 9757–9770.
25 A. Erfani, K. Szutkowski, C. P. Aichele and J. L. White, *Langmuir*, 2021, **37**, 858–866.
26 O. Vincent, B. Marguet and A. D. Stroock, *Langmuir*, 2017, **33**, 1655–1661.
27 A. Cihan, T. K. Tokunaga and J. T. Birkholzer, *Water Resour. Res.*, 2021, **57**, e2021WR029720.
28 H. Li, E. Fratini, W.-S. Chiang, P. Baglioni, E. Mamontov and S.-H. Chen, *Phys. Rev. E*, 2012, **86**, 061505.
29 R. Velasco, M. Pathak, P. Panja and M. Deo, in *Unconventional Resources Technology Conference, Austin, Texas, 24-26 July 2017*, Society of Exploration Geophysicists, American Association of Petroleum Geologists, Society of Petroleum Engineers, 2017, pp. 3248–3257.
30 K. Wu, Z. Chen, J. Li, X. Li, J. Xu and X. Dong, *Proc. Natl. Acad. Sci.*, 2017, **114**, 3358–3363.
31 P. Chiquet, D. Broseta and S. Thibeau, *Geofluids*, 2007, **7**, 112–122.
32 E. A. Al-Khdheeawi, S. Vialle, A. Barifcani, M. Sarmadivaleh and S. Iglauer, *Int. J. Greenh. Gas Control*, 2018, **68**, 216–229.
33 S. Iglauer, C. H. Pentland and A. Busch, *Water Resour. Res.*, 2015, **51**, 729–774.
34 S. Iglauer and A. Al-Yaseri, *Adv. Geo-Energy Res.*, 2021, **5**, 347–350.
35 M. J. Abdolhosseini Qomi, K. J. Krakowiak, M. Bauchy, K. L. Stewart, R. Shahsavari, D. Jagannathan, D. B. Brommer, A. Baronnet, M. J. Buehler, S. Yip, F.-J. Ulm, K. J. Van Vliet and R. J.-M. Pellenq, *Nat. Commun.*, 2014, **5**, 4960.

36 M. Bauchy, B. Wang, M. Wang, Y. Yu, M. J. Abdolhosseini Qomi, M. M. Smedskjaer, C. Bichara, F.-J. Ulm and R. Pellenq, *Acta Mater.*, 2016, **121**, 234–239.
37 A. Morshedifard, S. Masoumi and M. J. A. Qomi, *Nat. Commun.*, 2018, **9**, 1785.
38 F. Xi, S. J. Davis, P. Ciais, D. Crawford-Brown, D. Guan, C. Pade, T. Shi, M. Syddall, J. Lv, L. Ji, L. Bing, J. Wang, W. Wei, K.-H. Yang, B. Lagerblad, I. Galan, C. Andrade, Y. Zhang and Z. Liu, *Nat. Geosci.*, 2016, **9**, 880–883.
39 T. A. Boden, R. J. Andres and G. Marland, *Global, Regional, and National Fossil-Fuel CO2 Emissions (1751 - 2010) (V. 2013)*, Environmental System Science Data Infrastructure for a Virtual Ecosystem; Carbon Dioxide Information Analysis Center (CDIAC), Oak Ridge National Laboratory (ORNL), Oak Ridge, TN (United States), 2013.
40 L. Barcelo, J. Kline, G. Walenta and E. Gartner, *Mater. Struct.*, 2014, **47**, 1055–1065.
41 G. Rimmelé, V. Barlet-Gouédard, O. Porcherie, B. Goffé and F. Brunet, *Cem. Concr. Res.*, 2008, **38**, 1038–1048.
42 V. Barlet-Gouédard, G. Rimmelé, O. Porcherie, N. Quisel and J. Desroches, *Int. J. Greenh. Gas Control*, 2009, **3**, 206–216.
43 E. A. Chavez Panduro, M. Torsæter, K. Gawel, R. Bjørge, A. Gibaud, Y. Yang, S. Bruns, Y. Zheng, H. O. Sørensen and D. W. Breiby, *Environ. Sci. Technol.*, 2017, **51**, 9344–9351.
44 P. Renforth, *Nat. Commun.*, 2019, **10**, 1401.
45 P. J. M. Monteiro, G. Geng, D. Marchon, J. Li, P. Alapati, K. E. Kurtis and M. J. A. Qomi, *Cem. Concr. Res.*, 2019, **124**, 105806.
46 M. J. A. Qomi, M. Bauchy, F.-J. Ulm and R. J.-M. Pellenq, *J. Chem. Phys.*, 2014, **140**, 054515.
47 H. Erras-Hanauer, T. Clark and R. van Eldik, *Coord. Chem. Rev.*, 2003, **238–239**, 233–253.
48 M. J. Abdolhosseine Qomi, Q. R. S. Miller, S. Zare, H. T. Schaef, J. P. Kaszuba and K. M. Rosso, *Nat. Rev. Chem.*
49 S. Kerisit, J. H. Weare and A. R. Felmy, *Geochim. Cosmochim. Acta*, 2012, **84**, 137–151.
50 A. Botan, B. Rotenberg, V. Marry, P. Turq and B. Noetinger, *J. Phys. Chem. C*, 2010, **114**, 14962–14969.
51 S. Masoumi, S. Zare, H. Valipour and M. J. Abdolhosseini Qomi, *J. Phys. Chem. C*, 2019, **123**, 4755–4766.
52 S. Kerisit, E. J. Bylaska and A. R. Felmy, *Chem. Geol.*, 2013, **359**, 81–89.
53 Q. R. S. Miller, J. P. Kaszuba, S. N. Kerisit, H. Todd Schaef, M. E. Bowden, B. Peter McGrail and K. M. Rosso, *Environ. Sci. Nano*, 2020, **7**, 1068–1081.
54 E. Placencia-Gómez, S. N. Kerisit, H. S. Mehta, O. Qafoku, C. J. Thompson, T. R. Graham, E. S. Ilton and J. S. Loring, *Environ. Sci. Technol.*, 2020, **54**, 6888–6899.
55 C. J. Thompson, J. S. Loring, K. M. Rosso and Z. Wang, *Int. J. Greenh. Gas Control*, 2013, **18**, 246–255.
56 C. J. Thompson, P. F. Martin, J. Chen, P. Benezeth, H. T. Schaef, K. M. Rosso, A. R. Felmy and J. S. Loring, *Rev. Sci. Instrum.*, 2014, **85**, 044102.
57 J. S. Loring, C. J. Thompson, Z. Wang, A. G. Joly, D. S. Sklarew, H. T. Schaef, E. S. Ilton, K. M. Rosso and A. R. Felmy, *Environ. Sci. Technol.*, 2011, **45**, 6204–6210.
58 J. S. Loring, J. Chen, P. Bénézeth, O. Qafoku, E. S. Ilton, N. M. Washton, C. J. Thompson, P. F. Martin, B. P. McGrail, K. M. Rosso, A. R. Felmy and H. T. Schaef, *Langmuir*, 2015, **31**, 7533–7543.
59 J. S. Loring, Q. R. S. Miller, C. J. Thompson and H. T. Schaef, in *Science of Carbon Storage in Deep Saline Formations*, eds. P. Newell and A. G. Ilgen, Elsevier, 2019, pp. 63–88.
60 X. Zhang, A. S. Lea, A. M. Chaka, J. S. Loring, S. T. Mergelsberg, E. Nakouzi, O. Qafoku, J. J. De Yoreo, H. T. Schaef and K. M. Rosso, *Nat. Mater.*, 2021, 1–7.
61 Q. R. S. Miller, D. A. Dixon, S. D. Burton, E. D. Walter, D. W. Hoyt, A. S. McNeill, J. D. Moon, K. S. Thanthiriwatte, E. S. Ilton, O. Qafoku, C. J. Thompson, H. T. Schaef, K. M. Rosso and J. S. Loring, *J. Phys. Chem. C*, 2019, **123**, 12871–12885.
62 S. N. Kerisit, S. T. Mergelsberg, C. J. Thompson, S. K. White and J. S. Loring, *Environ. Sci. Technol.*, 2021, **55**, 12539–12548.

63 S. T. Mergelsberg, S. N. Kerisit, E. S. Ilton, O. Qafoku, C. J. Thompson and J. S. Loring, *Chem. Commun.*, 2020, **56**, 12154–12157.
64 R. S. Smith, Z. Li, Z. Dohnálek and B. D. Kay, *J. Phys. Chem. C*, 2014, **118**, 29091–29100.
65 S. A. Hamid, *Z. Krist.*, 1981, **154**, 189–198.
66 S. Peuble, M. Andreani, P. Gouze, M. Pollet-Villard, B. Reynard and B. Van de Moortele, *Chem. Geol.*, 2018, **476**, 150–160.
67 K. Marquardt and U. H. Faul, *Phys. Chem. Miner.*, 2018, **45**, 139–172.
68 T. Xing, W. Zhu, F. Fusseis and H. Lisabeth, *Solid Earth*, 2018, **9**, 879–896.
69 S. Erdmann, B. Scaillet, C. Martel and A. Cadoux, *J. Petrol.*, 2014, **55**, 2377–2402.
70 A. J. Luhmann, B. M. Tutolo, B. C. Bagley, D. F. R. Mildner, W. E. Seyfried Jr. and M. O. Saar, *Water Resour. Res.*, 2017, **53**, 1908–1927.
71 A. Silvestri, E. Ataman, A. Budi, S. L. S. Stipp, J. D. Gale and P. Raiteri, *Langmuir*, 2019, **35**, 16669–16678.
72 A. Silvestri, A. Budi, E. Ataman, M. H. M. Olsson, M. P. Andersson, S. L. S. Stipp, J. D. Gale and P. Raiteri, *J. Phys. Chem. C*, 2017, **121**, 24025–24035.
73 M. J. A. Qomi, M. Bauchy, F.-J. Ulm and R. J.-M. Pellenq, *J. Chem. Phys.*, 2014, **140**, 054515.
74 M. Youssef, R. J.-M. Pellenq and B. Yildiz, *J. Am. Chem. Soc.*, 2011, **133**, 2499–2510.
75 N. Spycher, K. Pruess and J. Ennis-King, *Geochim. Cosmochim. Acta*, 2003, **67**, 3015–3031.
76 L. W. Diamond and N. N. Akinfiev, *Fluid Phase Equilibria*, 2003, **208**, 265–290.
77 Q. Li, C. I. Steefel and Y.-S. Jun, *Environ. Sci. Technol.*, 2017, **51**, 10861–10871.
78 G. W. Scherer and B. Huet, *Int. J. Greenh. Gas Control*, 2009, **3**, 731–735.
79 A. Raoof, H. M. Nick, T. K. T. Wolterbeek and C. J. Spiers, *Int. J. Greenh. Gas Control*, 2012, **11**, S67–S77.
80 M. Pavlov, P. E. M. Siegbahn and M. Sandström, *J. Phys. Chem. A*, 1998, **102**, 219–228.
81 S. Chen and A. Navrotsky, *Am. Mineral.*, 2010, **95**, 112–117.
82 Y. Wu, H. L. Tepper and G. A. Voth, *J. Chem. Phys.*, 2006, **124**, 024503.
83 J. Vorholz, V. I. Harismiadis, B. Rumpf, A. Z. Panagiotopoulos and G. Maurer, *Fluid Phase Equilibria*, 2000, **170**, 203–234.
84 D. Hou, H. Ma, Y. Zhu and Z. Li, *Acta Mater.*, 2014, **67**, 81–94.
85 B. Li, N. Li, H. J. H. Brouwers, Q. Yu and W. Chen, *Constr. Build. Mater.*, 2020, **233**, 117347.
86 E. Nakouzi, A. G. Stack, S. Kerisit, B. A. Legg, C. J. Mundy, G. K. Schenter, J. Chun and J. J. De Yoreo, *J. Phys. Chem. C*, 2021, **125**, 1282–1291.
87 S. R. P. da Rocha, K. P. Johnston, R. E. Westacott and P. J. Rossky, *J. Phys. Chem. B*, 2001, **105**, 12092–12104.
88 B. Kvamme, A. Graue, T. Buanes, T. Kuznetsova and G. Ersland, *Int. J. Greenh. Gas Control*, 2007, **1**, 236–246.
89 T. Kuznetsova and B. Kvamme, *Phys. Chem. Chem. Phys.*, 2002, **4**, 937–941.
90 D. N. Espinoza and J. C. Santamarina, *Water Resour. Res.*, , DOI:10.1029/2009WR008634.
91 H. J?nsson, G. Mills and K. W. Jacobsen, in *Classical and Quantum Dynamics in Condensed Phase Simulations*, WORLD SCIENTIFIC, 1998, pp. 385–404.
92 H. T. Schaef, J. S. Loring, V.-A. Glezakou, Q. R. S. Miller, J. Chen, A. T. Owen, M.-S. Lee, E. S. Ilton, A. R. Felmy, B. P. McGrail and C. J. Thompson, *Geochim. Cosmochim. Acta*, 2015, **161**, 248–257.
93 J. S. Loring, E. S. Ilton, J. Chen, C. J. Thompson, P. F. Martin, P. Bénézeth, K. M. Rosso, A. R. Felmy and H. T. Schaef, *Langmuir*, 2014, **30**, 6120–6128.
94 U. Burghaus, *Prog. Surf. Sci.*, 2014, **89**, 161–217.
95 A. Stirling, *J. Phys. Chem. B*, 2011, **115**, 14683–14687.
96 M. T. Nguyen, M. H. Matus, V. E. Jackson, V. T. Ngan, J. R. Rustad and D. A. Dixon, *J. Phys. Chem. A*, 2008, **112**, 10386–10398.
97 S. Yamabe and N. Kawagishi, *Theor. Chem. Acc.*, 2011, **130**, 909–918.
98 A. Stirling and I. Pápai, *J. Phys. Chem. B*, 2010, **114**, 16854–16859.

99 M. G. Martin; 'MCCCS Towhee: a tool for Monte Carlo molecular simulation', Mol. Simulat. 39 1212-1222 (2013), (accessed 29 September 2018).
100 G. C. A. M. Mooij, D. Frenkel and B. Smit, *J. Phys. Condens. Matter*, 1992, **4**, L255.
101 H. J. C. Berendsen, J. P. M. Postma, W. F. van Gunsteren and J. Hermans, in *Intermolecular Forces: Proceedings of the Fourteenth Jerusalem Symposium on Quantum Chemistry and Biochemistry Held in Jerusalem, Israel, April 13–16, 1981*, ed. B. Pullman, Springer Netherlands, Dordrecht, 1981, pp. 331–342.
102 J. G. Harris and K. H. Yung, *J. Phys. Chem.*, 1995, **99**, 12021–12024.
103 R. T. Cygan, J.-J. Liang and A. G. Kalinichev, *J. Phys. Chem. B*, 2004, **108**, 1255–1266.
104 M. J. A. Qomi, K. J. Krakowiak, M. Bauchy, K. L. Stewart, R. Shahsavari, D. Jagannathan, D. B. Brommer, A. Baronnet, M. J. Buehler, S. Yip, F.-J. Ulm, K. J. V. Vliet and R. J.-M. Pellenq, *Nat. Commun.*, 2014, **5**, 4960.
105 H. Yan, C. Park, G. Ahn, S. Hong, D. T. Keane, C. Kenney-Benson, P. Chow, Y. Xiao and G. Shen, *Geochim. Cosmochim. Acta*, 2014, **145**, 268–280.
106 H. E. King, M. Stimpfl, P. Deymier, M. J. Drake, C. R. A. Catlow, A. Putnis and N. H. de Leeuw, *Earth Planet. Sci. Lett.*, 2010, **300**, 11–18.
107 N. H. de Leeuw, S. C. Parker, C. R. A. Catlow and G. D. Price, *Phys. Chem. Miner.*, 2000, **27**, 332–341.
108 S. Plimpton, *J. Comput. Phys.*, 1995, **117**, 1–19.
109 H. J. C. Berendsen, J. R. Grigera and T. P. Straatsma, *J. Phys. Chem.*, 1987, **91**, 6269–6271.
110 R. T. Cygan, V. N. Romanov and E. M. Myshakin, *J. Phys. Chem. C*, 2012, **116**, 13079–13091.
111 G. A. Tribello, M. Bonomi, D. Branduardi, C. Camilloni and G. Bussi, *Comput. Phys. Commun.*, 2014, **185**, 604–613.
112 R. Shahsavari, R. J.-M. Pellenq and F.-J. Ulm, *Phys. Chem. Chem. Phys.*, 2011, **13**, 1002–1011.
113 S. Kumar, J. M. Rosenberg, D. Bouzida, R. H. Swendsen and P. A. Kollman, *J. Comput. Chem.*, 1992, **13**, 1011–1021.
114 A. Funk and H. F. R. Trettin, *Ind. Eng. Chem. Res.*, 2013, **52**, 2168–2173.
115 R. Car and M. Parrinello, *Phys. Rev. Lett.*, 1985, **55**, 2471–2474.
116 J. VandeVondele and J. Hutter, *J. Chem. Phys.*, 2007, **127**, 114105.
117 S. Goedecker, M. Teter and J. Hutter, *Phys. Rev. B*, 1996, **54**, 1703–1710.
118 C. Hartwigsen, S. Goedecker and J. Hutter, *Phys. Rev. B*, 1998, **58**, 3641–3662.
119 M. Krack, *Theor. Chem. Acc.*, 2005, **114**, 145–152.
120 J. P. Perdew, K. Burke and M. Ernzerhof, *Phys. Rev. Lett.*, 1996, **77**, 3865–3868.
121 Y. Zhang and W. Yang, *Phys. Rev. Lett.*, 1998, **80**, 890–890.
122 S. Grimme, J. Antony, S. Ehrlich and H. Krieg, *J. Chem. Phys.*, 2010, **132**, 154104.
123 L. Goerigk, A. Hansen, C. Bauer, S. Ehrlich, A. Najibi and S. Grimme, *Phys. Chem. Chem. Phys.*, 2017, **19**, 32184–32215.
124 T. Gould, *Phys. Chem. Chem. Phys.*, 2018, **20**, 27735–27739.
125 S. A. Trygubenko and D. J. Wales, *J. Chem. Phys.*, 2004, **120**, 2082–2094.
126 G. Henkelman and H. Jónsson, *J. Chem. Phys.*, 2000, **113**, 9978–9985.
127 G. Henkelman, B. P. Uberuaga and H. Jónsson, *J. Chem. Phys.*, 2000, **113**, 9901–9904.